

Solid-State ^{45}Sc NMR Studies of $\text{Cp}^*_2\text{Sc}-\text{OR}$ ($\text{R} = \text{CMe}_2\text{CF}_3$, $\text{CMe}(\text{CF}_3)_2$, $\text{C}(\text{CF}_3)_3$, SiPh_3) and Relationship to the Structure of Cp^*_2Sc -Sites Supported on Partially Dehydroxylated Silica

Damien B. Culver,[‡] Winn Huynh,[‡] Hosein Tafazolian, and Matthew P. Conley*



Cite This: *Organometallics* 2020, 39, 1112–1122



Read Online

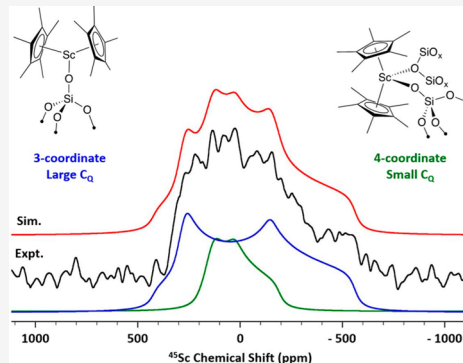
ACCESS |

Metrics & More

Article Recommendations

Supporting Information

ABSTRACT: $\text{Cp}^*_2\text{Sc}-\text{OR}$ ($\text{R} = \text{CMe}_2\text{CF}_3$, $\text{CMe}(\text{CF}_3)_2$, $\text{C}(\text{CF}_3)_3$, SiPh_3) was synthesized to determine how the alkoxide affects the quadrupole coupling (C_Q) obtained from solid-state $^{45}\text{Sc}\{^1\text{H}\}$ NMR spectroscopy. These alkoxides are characterized by large (>29 MHz) C_Q values, which are similar to C_Q values obtained for $\text{Cp}^*_2\text{Sc}-\text{R}$ ($\text{R} = \text{Me, Et, Ph}$) and $\text{Cp}^*_2\text{Sc}-\text{X}$ ($\text{X} = \text{F, Cl, Br, I}$) but significantly larger than C_Q values obtained for $\text{Cp}^*_2\text{ScX}(\text{THF})$. The NMR properties from these alkoxides were used to understand the NMR properties of Cp^*_2Sc -supported on silica partially dehydroxylated at 700 °C. This material contains two species from the solid-state $^{45}\text{Sc}\{^1\text{H}\}$ NMR spectra assigned to $\text{Cp}^*_2\text{ScOSi}\equiv$ (**5a**) and $\text{Cp}^*_2\text{Sc}(\text{OSi}\equiv)\text{O}(\text{SiO}_x)_2$ (**5b**). The solid-state $^{45}\text{Sc}\{^1\text{H}\}$ NMR spectrum of **5a** is considerably broader than **5b**, which relates to the magnitude of the quadrupolar coupling (C_Q) in these two different sites. Density functional theory (DFT) optimized structures of $\text{Cp}^*_2\text{Sc}-\text{OR}$ and small cluster approximations of **5a** and **5b** follow similar trends as the experimental C_Q values for this family of organoscandium complexes. Analysis of the origin of C_Q using DFT methods shows that σ - and π -bonding orbitals from the Sc–O bond in $\text{Cp}^*_2\text{Sc}-\text{OR}$ and **5a** are major contributors to C_Q , whereas different orbitals contribute to C_Q in **5b**. These studies show that quadrupolar solid-state NMR spectroscopy can distinguish between surface sites on partially dehydroxylated silica.



INTRODUCTION

Many of the largest scale catalytic reactions in industry use heterogeneous catalysts. These catalysts are usually thought to contain organometallic intermediates, either on a metal or an oxide surface.¹ Understanding these catalysts at a molecular level is challenging because these complex materials often have very low active site loadings, which complicates analysis of spectroscopic data when attempting to determine active site structure. For these reasons, introducing molecular precision on oxides surfaces is a long-term interdisciplinary challenge. One of the most familiar ways to address this challenge is to incorporate organometallic complexes onto a partially dehydroxylated support, Scheme 1.^{2–9}

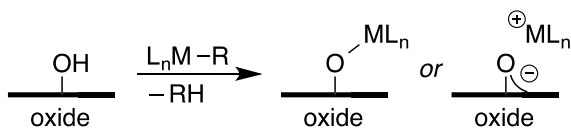
The proton transfer reaction in Scheme 1 results in formation of alkane and a well-defined supported organometallic that can form a covalent $\text{M}-\text{O}_x$ ($\text{O}_x = \text{surface oxygen}$)

or an electrophilic $\text{M}--\text{O}_x$ ion pair. The nature of the support controls the formation of $\text{M}-\text{O}_x$ or $\text{M}--\text{O}_x$ ion pairs. Neutral supports (SiO_2 , Al_2O_3) used in this reaction tend to form $\text{M}-\text{O}_x$. More Bronsted acidic supports, such as zeolites or sulfated oxides, usually form $\text{M}--\text{O}_x$ ion pairs.^{10–21}

The most common method to determine structure in well-defined organometallics supported on oxides is solid-state NMR spectroscopy.^{22,23} Magic angle spinning (MAS) is now a common technique, and moderate spinning speeds (~ 10 kHz) are sufficient to suppress some of the anisotropic interactions in the solid state that can complicate analysis of NMR spectra. At these spinning speeds, the spectra of typical spin 1/2 nuclei (^{31}P , ^{13}C , ^{29}Si , etc) usually show isotropic chemical shift values that can be interpreted in similar ways to signals obtained from solution NMR spectra.

A few representative examples showing how analysis of isotropic NMR chemical shift can give information about the structure of surface species are shown in Figure 1. The isotropic ^{29}Si NMR chemical shift is sensitive to the nature of

Scheme 1. Reaction of Generic Organometallic with Oxide Surface To Form Either $\text{M}-\text{O}_x$ or $\text{M}--\text{O}_x$ Ion Pairs



Special Issue: Organometallic Chemistry at Various Length Scales

Received: December 11, 2019

Published: February 26, 2020

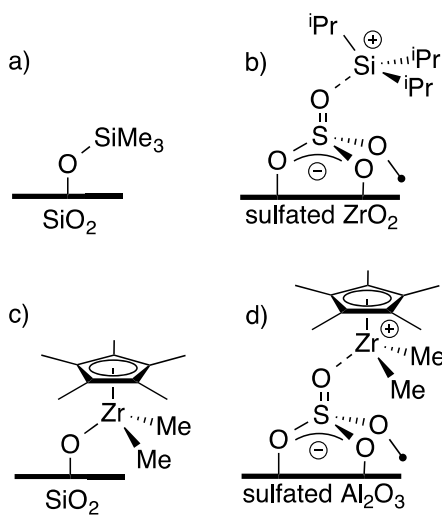


Figure 1. Representative examples of well-defined surface species that show pronounced differences in the isotropic ^{29}Si chemical shift (a, b) or ^{13}C chemical shift (c, d).

the substituents connected to silicon.²⁴ Alkylsilanes have ^{29}Si NMR chemical shifts at ~ 0 ppm, while silylum ions (R_3Si^+) paired to weakly coordinating anions have chemical shifts between ~ 90 and 140 ppm.^{25–27} This trend also applies to organosilanes supported on oxides. Alkylsilanes react with silica to form $\equiv\text{SiO}-\text{SiR}_3$ (Figure 1a).²⁸ The ^{29}Si cross-polarization magic angle spinning (CPMAS) NMR spectrum of $\equiv\text{SiO}-\text{SiR}_3$ contains signals at ~ 14 ppm.^{29–31} This chemical shift is close to the ^{29}Si NMR chemical shift of silyl ethers in solution, and is consistent with formation of $\equiv\text{SiO}-\text{SiR}_3$, and the observation that weakly acidic supports do not form ion pairs. Sulfated zirconium oxide reacts with allyltriisopropylsilane to form $[\text{iPr}_3\text{Si}][\text{SZO}]$ ion pairs (Figure 1b).³² The ^{29}Si CPMAS NMR spectrum of $[\text{iPr}_3\text{Si}][\text{SZO}]$ contains a major signal at 53 ppm, which is ~ 10 ppm downfield from the ^{29}Si NMR chemical shift of iPr_3SiOTf and is consistent with the formation of a surface ion pair. Recent reports of iPr_3Si -sites supported on silica surfaces containing weakly coordinating anions contained a ^{29}Si NMR signal at 70 ppm, to date the most deshielded ^{29}Si NMR signal for a R_3Si -site supported on an oxide.³³

Similar conclusions are supported by analysis of ^{13}C NMR chemical shifts. $\equiv\text{SiO}-\text{ZrCp}^*(\text{Me})_2$, shown in Figure 1c, contains a signal at 39 ppm for the Zr-Me.³⁴ Cp^*ZrMe_3 supported on sulfated alumina forms $[\text{Cp}^*\text{ZrMe}_2][\text{oxide}]$ ion pairs (Figure 1d), which is supported by a downfield shift of the Zr-Me signal ($\delta = 49$) and extended X-ray adsorption fine structure (EXAFS) studies.²¹

Though solid-state NMR is an indispensable technique in studies of surface species, there are certain ambiguities that cannot be resolved using this method. For example, $\text{Ta}(=\text{CH}^t\text{Bu})(\text{CH}_2^t\text{Bu})_3$ supported on silica partially dehydroxylated at $700\text{ }^\circ\text{C}$ (SiO_{2-700}) forms $\equiv\text{SiO}-\text{Ta}(=\text{CH}^t\text{Bu})(\text{CH}_2^t\text{Bu})_2$, results supported by extensive solid-state NMR studies.³⁵ However, EXAFS analysis showed that a significant fraction of $\equiv\text{SiO}-\text{Ta}(=\text{CH}^t\text{Bu})(\text{CH}_2^t\text{Bu})_2$ also contains a siloxane bridge ligand, Figure 2a. Several early transition metal or lanthanide complexes supported on silica show similar behavior^{36–39} and in NMR data of spin 1/2 nuclei usually

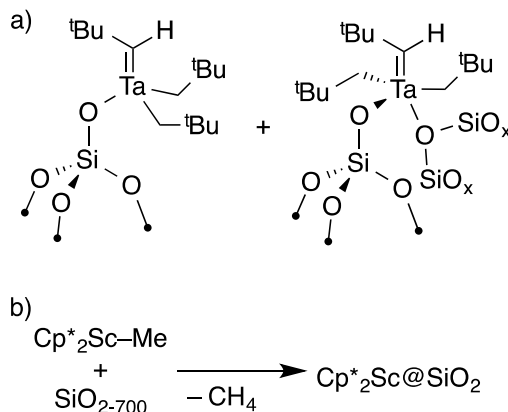


Figure 2. Two products of the reaction between partially dehydroxylated silica and $\text{Ta}(=\text{CH}^t\text{Bu})(\text{CH}_2^t\text{Bu})_3$; $\equiv\text{SiO}-\text{Ta}(=\text{CH}^t\text{Bu})(\text{CH}_2^t\text{Bu})_2$ shown on the left and $\equiv\text{SiO}-\text{Ta}(=\text{CH}^t\text{Bu})(\text{CH}_2^t\text{Bu})_2(\text{O}(\text{SiO}_x)_2)$ is shown on the right in (a). The reaction of partially dehydroxylated silica and Cp^*ScMe , the objective of this study (b).

cannot distinguish between the presence or absence of a siloxane bridge ligand.⁴⁰

This paper describes the reaction of Cp^*ScMe , a monomeric C_{2v} bent metallocene,⁴¹ with partially dehydroxylated silica (Figure 2b), and the application of solid-state $^{45}\text{Sc}\{^1\text{H}\}$ NMR spectroscopy to determine the structures of surface sites. Scandium has one NMR active nucleus (^{45}Sc , $I = 7/2$, $\gamma = 6.5081 \times 10^7 \text{ rad T}^{-1} \text{ s}^{-1}$, 100% abundant) and is quadrupolar. Quadrupolar solid-state NMR of solids is a powerful technique to obtain information about structure⁴² and is also useful in studying supported organometallics.^{43–47} Given these characteristics, ^{45}Sc NMR may be able to distinguish between products that coordinate to siloxane bridges and those that do not coordinate to siloxane bridges.

Quadrupolar nuclei contain nonspherically symmetric distributions of positive charge. From a practical perspective, this is most commonly manifested as broad signals in solution NMR spectra. In solution, molecules tumble, which averages NMR interactions that depend on the orientation of the nuclear spins with respect to the external magnetic field (\mathbf{B}_0). This is not the case in the solid-state, and spatially dependent NMR interactions can often be measured directly, provided that dynamics are slow on the NMR time scale. In quadrupolar nuclei, the dominant spatially dependent NMR interaction is between the electric field gradient (EFG) tensor and the quadrupole moment of the nucleus. The EFG is a traceless second-rank tensor (V , eq 1). The three principal components of the EFG tensor are ordered $|V_{33}| \geq |V_{22}| \geq |V_{11}|$. The quadrupolar coupling constant (C_Q) describes the magnitude of V_{33} , eq 2, where e = fundamental charge; Q = nuclear quadrupole moment; h = Planck's constant. Experimental C_Q can be extracted from solid-state NMR data. The magnitude of C_Q is usually much larger than typical MAS speeds (~ 10 kHz), which can complicate analysis of NMR spectra under MAS unless very fast spinning speeds are accessible (> 50 kHz). Acquisition of static NMR spectra using low RF fields in combination with frequency steps,⁴⁸ or pulse sequences containing echo-trains,⁴⁹ results in powder patterns whose properties can be simulated using commercially available software to extract C_Q from experimental data:

$$\mathbf{V} = \begin{vmatrix} V_{11} & 0 & 0 \\ 0 & V_{22} & 0 \\ 0 & 0 & V_{33} \end{vmatrix} \quad (1)$$

$$C_Q = \frac{e^2 Q V_{33}}{h} \quad (2)$$

C_Q is sensitive to symmetry, perturbations of core orbitals, and population of valence bonding orbitals.^{42,50,51} A summary of C_Q values for available $\text{Cp}^*{}^2\text{Sc}$ -complexes is shown in Figure 3. The base-free $\text{Cp}^*{}^2\text{Sc}-\text{X}$ ($\text{X} = \text{F}, \text{Cl}, \text{Br}, \text{I}$) and

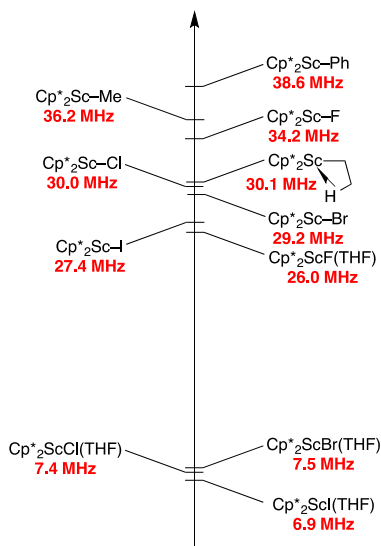


Figure 3. Summary of available C_Q values for $\text{Cp}^*{}^2\text{Sc}$ -complexes.

$\text{Cp}^*{}^2\text{Sc}-\text{R}$ ($\text{R} = \text{Me}, \text{Et}, \text{Ph}$) are characterized by relatively large C_Q values >27 MHz. These values are larger than scandium complexes that have higher symmetry than these metallocenes⁵² or crystalline porous materials⁵³ but smaller than the $\text{C}_3\text{Sc}[\text{N}(\text{SiMe}_3)]_3$ amide ($C_Q = 66.2$ MHz).⁵⁴ Figure 3 shows how subtle changes in the $\text{Cp}^*{}^2\text{Sc}$ -structure affect C_Q . For example, $\text{Cp}^*{}^2\text{Sc}-\text{Me}$ has a larger C_Q than $\text{Cp}^*{}^2\text{Sc}-\text{Et}$ because the latter contains a β -agostic structure (Figure 3).⁵⁵ More dramatic differences in C_Q were observed in studies of $\text{Cp}^*{}^2\text{Sc}-\text{X}$ and $\text{Cp}^*{}^2\text{ScX(THF)}$ ($\text{X} = \text{F}, \text{Cl}, \text{Br}, \text{I}$). The base-free halides have much larger C_Q values than the THF adducts.⁵⁶ Density functional theory (DFT) studies of these compounds showed that the smaller C_Q values for the THF adducts are due to the higher symmetry at Sc, which results in some degree of π -bonding from the halide to scandium.

The solid-state $^{45}\text{Sc}\{^1\text{H}\}$ NMR data shown in Figure 3 is a rough empirical aid for the interpretation of $^{45}\text{Sc}\{^1\text{H}\}$ NMR data of $\text{Cp}^*{}^2\text{ScMe}$ supported on partially dehydroxylated silica. Formation of $\text{Cp}^*{}^2\text{ScOSi}\equiv$, a terminal siloxy surface species, should result in a large C_Q . Coordination of a siloxane bridge, which is reasonable based on the well-defined organometallics mentioned above, would form $\text{Cp}^*{}^2\text{Sc}(\text{OSi}\equiv)\text{O}(\text{SiO}_x)_2$, which is expected to have a smaller C_Q than the terminal siloxy surface species.

DFT methods accurately predict C_Q and can decompose the C_Q into individual natural localized molecular orbitals to give insights into the origin of this spectroscopic observable.^{50,51,57} DFT descriptions of amorphous supports, such as SiO_2 , are complex.⁵⁸ However, several studies showed that C_Q depends

only on the first coordination sphere and that small cluster models give predicted C_Q values close to experimental values for a given coordination environment.^{43,59,60} Simple approximations of a silica surface, such as the $-\text{OSi}(\text{OMe})_3$ ligand or related simple siloxy models, also predict reactivity patterns and spectroscopic properties of organometallics supported on silica.^{61–64} This article shows that the reaction of $\text{Cp}^*{}^2\text{ScMe}$ on silica dehydroxylated at 700 °C (SiO_{2-700}) generates two surface species by solid-state $^{45}\text{Sc}\{^1\text{H}\}$ NMR spectroscopy. Analysis of solid-state $^{45}\text{Sc}\{^1\text{H}\}$ NMR data for terminal alkoxide complexes, formed in the reaction of $\text{Cp}^*{}^2\text{ScMe}$ and ROH, shows that these complexes have similar C_Q values as the base free scandocene complexes in Figure 3. DFT calculations of these molecular alkoxides reproduce the structures of these complexes and predict scandium C_Q values close to experimental values. This benchmarks the DFT studies of the small cluster models for $\text{Cp}^*{}^2\text{ScOSi}\equiv$ and $\text{Cp}^*{}^2\text{Sc}(\text{OSi}\equiv)\text{O}(\text{SiO}_x)_2$ shown in Figure 4. This study shows that

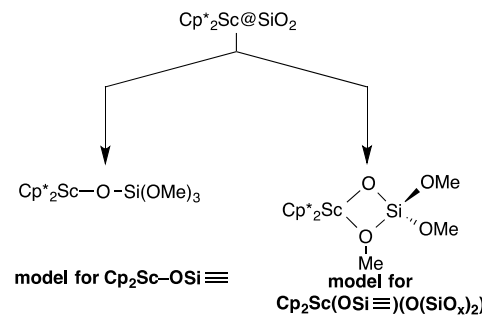


Figure 4. DFT models for $\text{Cp}^*{}^2\text{ScOSi}\equiv$ and $\text{Cp}^*{}^2\text{Sc}(\text{OSi}\equiv)\text{O}(\text{SiO}_x)_2$.

the two reaction products in $\text{Cp}^*{}^2\text{Sc@SiO}_2$ are $\text{Cp}^*{}^2\text{ScOSi}\equiv$ and $\text{Cp}^*{}^2\text{Sc}(\text{OSi}\equiv)\text{O}(\text{SiO}_x)_2$ from solid-state $^{45}\text{Sc}\{^1\text{H}\}$ NMR spectroscopy. NLMO decomposition of the origins of C_Q in these two clusters shows that the geometry differences in the κ^1 - and κ^2 -coordination modes of $-\text{OSi}(\text{OMe})_3$ result in different bonding orbital contributions to V_{33} .

EXPERIMENTAL SECTION

General Considerations. All manipulations were performed under an inert atmosphere of dinitrogen or argon. Benzene-d₆ and cyclohexane-d₁₂ were purchased from Cambridge Isotope laboratories and dried over sodium/benzophenone, distilled under vacuum, and stored inside an inert atmosphere glovebox. Pentane and toluene were dried over sodium/benzophenone, degassed, and distilled under vacuum. Nonane, 1,1,1-trifluoro-2-methyl-2-propanol, and 1,1,1,3,3-hexafluoro-2-methyl-2-propanol were purchased from standard suppliers, dried over calcium hydride, and distilled under vacuum prior to use. Triphenylsilanol was sublimed under vacuum prior to use. Methylolithium in Et₂O was purchased from Sigma-Aldrich. Synthesis of $\text{Cp}^*{}^2\text{ScCl}$ and $\text{Cp}^*{}^2\text{ScMe}$ was reported previously.⁴¹

Aerosil-200 was obtained from Degussa. Aerosil-200 dehydroxylated at 700 °C (SiO_{2-700}) was prepared by suspending the silica in excess water and drying the slurry under static air at 120 °C in an oven for 1 day. The resulting monolith was crushed and sieved to give 250–425 μm size silica aggregates. This material was loaded into a quartz tube containing an adapter with a Teflon stopcock to attach to a high vacuum line, placed in a tube furnace, heated under static air at 500 °C (5 °C min⁻¹) for 4 h, and placed under vacuum on a diffusion pump vacuum line for 12 h. While under vacuum, the temperature was increased to 700 °C (5 °C min⁻¹) and its temperature maintained for 4 h. After this time, the Teflon stopcock was sealed, and the tube

Table 1. ^{45}Sc NMR Parameters for 1–5 Extracted from Simulations in Figures 6 and 7^a

	δ_{iso} (ppm)	C_Q (MHz)	η	Ω (ppm)	κ	α (deg)	β (deg)	γ (deg)
1	65(5)	31.6(1)	0.80(1)	290(20)	0.50(1)	95(5)	90(1)	90(1)
2	99(1)	30.5(1)	0.63(2)	270(10)	0.19(4)	106(4)	88(2)	88(3)
3	133(1)	29.2(2)	0.33(1)	375(3)	0.25(5)	103(2)	96(6)	78(3)
4	94(2)	35.1(1)	0.77(1)	239(3)	0.5(1)	108(5)	89(2)	90(1)
5a	135(15)	35.4(4)	0.60(5)	315(20)	0.90(8)	90(1)	90(1)	90(1)
5b	95(5)	21.9(3)	0.77(3)	150(15)	0.65(9)	90(1)	90(1)	90(1)

^aValues reported in the table are averages from simulations of experimental NMR data acquired at 9.4 and 14.1 T. Numbers in parentheses give the deviation from the average from these data.

was cooled to ambient temperature. The partially dehydroxylated silica was stored in an Ar filled glovebox and contains 0.26 mmol OH g⁻¹.

NMR Spectroscopy. Solution phase ^1H , $^{13}\text{C}\{^1\text{H}\}$, $^{19}\text{F}\{^1\text{H}\}$, and $^{45}\text{Sc}\{^1\text{H}\}$ NMR spectroscopy were acquired on a Bruker 300 Avance spectrometer, Varian 500, or Bruker 600 Avance spectrometer. ^1H and ^{13}C NMR spectra were referenced to the NMR solvent residual peak. ^{19}F NMR spectra were referenced to C_6F_6 (−163.9 ppm) external standard. ^{45}Sc NMR spectra were referenced to 0.11 M ScCl_3 in 0.1 M aqueous HCl solution (0.0 ppm).

Solid state NMR spectra were recorded in 4 mm zirconia rotors packed inside an inert atmosphere glovebox, and acquired on a Bruker 400 Avance III or a Bruker Neo-600 NMR spectrometer. The ^{13}C CP/MAS NMR spectra were recorded with a 2 ms contact time and a 2 s relaxation delay. Static $^{45}\text{Sc}\{^1\text{H}\}$ NMR spectra were recorded with a Hahn-echo pulse sequence, with full echo detection ($\pi/2 - \tau - \pi - \text{acq}$). Echo delays (τ) were 100–150 μs . All analytical simulations of solid state spectra were performed in TopSpin using Sola line shape analysis.

General Synthesis of $\text{Cp}^*_2\text{Sc-OR}$. Cp^*_2ScMe (200–500 mg, 0.6–1.5 mmol) was dissolved in toluene (5–15 mL) and cooled to 0 °C. The alcohol (1.05–1.1 equiv) was added dropwise to the solution by syringe. After addition, the reaction was stirred at 0 °C for 10 min, then 20 min at room temperature. The volatiles were removed under vacuum, and a minimal amount of pentane was added by cannula to dissolve the residue. Recrystallization from pentane at −20 °C results in yellow crystals for compounds 1–3. Yields and analytical data for the individual compounds are given below. The solid-state ^{45}Sc NMR data are given in below and summarized in Table 1. Results for C_6H elemental analyses of 1–4 did not yield satisfactory results, possibly due to the sensitivity of these compounds. Elemental analysis data are given in the Supporting Information (Table S1).

$\text{Cp}^*_2\text{Sc-OCMe}_2\text{CF}_3$ (1). Yield: 62%. ^1H NMR (C_6D_6 , 300 MHz): δ 1.89 (s, 30 H, CpMe), 1.56 (q, $^4J_{\text{HF}} = 1$ Hz, 6 H, OCMe_2CF_3). $^{13}\text{C}\{^1\text{H}\}$ NMR (C_6D_{12} , 151 MHz): 129.4 (q, $^1J_{\text{CF}} = 289$ Hz, OCMe_2CF_3), 122.5 (CpMe), 78.7 (q, $^2J_{\text{CF}} = 27$ Hz, CCF_3Me_2), 29.2 (OCMe_2CF_3), 12.6 (CpMe). $^{19}\text{F}\{^1\text{H}\}$ NMR (C_6D_6 , 282 MHz): δ −82.0 (s). ^{45}Sc NMR (C_6D_6 , 73 MHz): δ 70 (br s).

$\text{Cp}^*_2\text{Sc-OCMe}(\text{CF}_3)_2$ (2). Yield: 10%. ^1H NMR (C_6D_6 , 300 MHz): δ 1.83 (s, 30 H, CpMe), 1.78 (sept, $^4J_{\text{HF}} = 1.5$ Hz, 6 H, $\text{OCMe}(\text{CF}_3)_2$). $^{13}\text{C}\{^1\text{H}\}$ NMR (C_6D_{12} , 126 MHz): 126.3 (q, $^1J_{\text{CF}} = 289$ Hz, $\text{OCMe}(\text{CF}_3)_2$), 123.8 (CpMe), 82.9 (m, CCF_3Me_2), 23.2 ($\text{OCMe}(\text{CF}_3)_2$), 12.7 (bs, CpMe). $^{19}\text{F}\{^1\text{H}\}$ NMR (C_6D_6 , 282 MHz): δ −77.5 (s). ^{45}Sc NMR (C_6D_6 , 73 MHz): δ 89.

$\text{Cp}^*_2\text{Sc-OC}(\text{CF}_3)_3$ (3). Yield: 26%. ^1H NMR (C_6D_6 , 300 MHz): δ 1.79 (s, 30 H, CpMe). $^{13}\text{C}\{^1\text{H}\}$ NMR (C_6D_{12} , 151 MHz): δ 125.6 (s, CpMe), 123.7 (q, $^1J_{\text{CF}} = 295$ Hz, $\text{OC}(\text{CF}_3)_3$), 86.6 (br m, $\text{OC}(\text{CF}_3)_3$), 12.4 (s, CpMe). $^{19}\text{F}\{^1\text{H}\}$ NMR (C_6D_6 , 282 MHz): δ −73.2 (s). ^{45}Sc NMR (C_6D_6 , 73 MHz): δ 118 (br s).

$\text{Cp}^*_2\text{Sc-OSiPh}_3$ (4). This compound was synthesized with a slight modification of the generally synthesis. Triphenylsilanol (1.05 equiv) was dissolved in toluene and added to Cp^*_2ScMe by syringe. Yield: 48%. ^1H NMR (C_6D_6 , 300 MHz): δ 7.28–7.31 (m, 6 H, ArH), 7.89–7.92 (m, 9 H, ArH), 1.82 (s, 30 H, CpMe). $^{13}\text{C}\{^1\text{H}\}$ NMR (C_6D_6 , 151 MHz): δ 142.1 (s, Ph), 137.2 (s, Ph), 129.7 (s, Ph), 128.3 (s, Ph),

122.7 (s, CpMe), 12.5 (s, CpMe). $^{45}\text{Sc}\{^1\text{H}\}$ NMR (C_6D_6 , 73 MHz): δ 289 (br s).

Synthesis of 5. SiO_{2-700} (0.2 g, 0.052 mmol OH) and Cp^*_2ScMe (18 mg, 0.055 mmol) were loaded into a double Schlenk in an argon filled glovebox. The double Schlenk was connected to a high vacuum line, evacuated, and pentane (5 mL) was condensed onto the solids at 77 K. The slurry was warmed to room temperature and gently stirred for 1 h. Then the solution was filtered to the other arm of the double Schlenk. The derivatized silica was washed by condensing solvent from the other arm of the double Schlenk at 77 K, warming to room temperature, stirring for 2 min, and filtering the solvent back to the other side of the flask. This was repeated two times. The volatiles were transferred to a flask containing a Teflon stopcock at 77 K. Analysis of the volatiles by gas chromatography shows that 0.23 mmol/g of CH_4 are released during the reaction. The pale yellow solid was dried under diffusion pump vacuum for 1 h and was stored in a glovebox freezer at −20 °C. Solid state NMR: ^1H MAS NMR (600 MHz): δ 2.9–2.5 (CpMe). $^{13}\text{C}\{^1\text{H}\}$ CP/MAS NMR (151 MHz): δ 121.5 (CpMe), 9.6 (CpMe); and $^{29}\text{Si}\{^1\text{H}\}$ CP/MAS NMR (119 MHz): δ −106 (SiO_2) ppm. Elemental analysis for 5: C 5.61, H 0.49. ^{45}Sc NMR data are shown below and summarized in Table 1.

Computational Details. The geometries of 1–4, 6a, and 6b were optimized with Gaussian 09 using the B3LYP functional and the 6-311G** basis set on scandium and the 6-31G** basis set on all other atoms. Frequency calculations at the same level of theory produced no imaginary frequencies, indicating an energy minimum equilibrium structure. The NMR parameters of 1–4, 6a, and 6b were modeled in the Amsterdam Density Functional suite of programs at the B3LYP/DZ, Si(DZP) level of theory using the GIAO method. The calculated isotropic chemical shift was referenced to geometry-optimized $\text{Sc}(\text{H}_2\text{O})_6^{3+}$ at the same level of theory, which was used previously to reference ^{45}Sc chemical shift calculations.⁵² Contributions of each natural localized molecular orbital (NLMO) to the C_Q were calculated at the same level of theory.⁵⁰ The EFG tensor plots were plotted using TensorView.⁶⁵

RESULTS AND DISCUSSION

Synthesis of $\text{Cp}^*_2\text{Sc-OR}$ (R = CMe_2CF_3 , $\text{CMe}(\text{CF}_3)_2$, $\text{C}(\text{CF}_3)_3$, SiPh_3) and $\text{Cp}^*_2\text{ScOSi}\equiv$. The reaction of Cp^*_2ScMe with fluorinated alcohols and triphenylsilanol form methane and $\text{Cp}^*_2\text{Sc-OR}$ (R = CMe_2CF_3 (1), $\text{CMe}(\text{CF}_3)_2$ (2), $\text{C}(\text{CF}_3)_3$ (3), SiPh_3 (4)), Scheme 2. The products were isolated as crystalline (1 and 3) or microcrystalline (2 and 4) solids in moderate yields.

The solid-state structures of 1 and 3 are shown in Figure 5. 3 crystallizes with three nearly identical molecules in the unit cell. 1 and 3 adopt bent C_{2v} structures that are typical for d^0 metallocenes. The Sc–O distance in 1 is 1.9481(8) Å, which is shorter than the average Sc–O distance in 3 (2.033(1) Å). In both cases, the Sc–O–C bond angle is nearly linear (175.16(7)° in 1 and 173.5(1)° in 3). The Cp^* –Sc bond distances in 1 are 2.2031(6) and 2.2088(6) Å, and the Cp^* –Sc– Cp^* angle is 135.26(2)°. In 3, the average Cp^* –Sc– Cp^* angle is 133.9(1)°, and the average Cp^* –Sc bond distances are

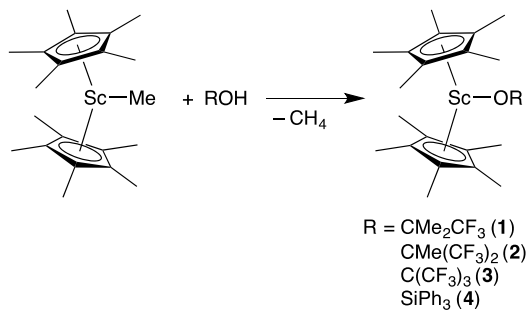
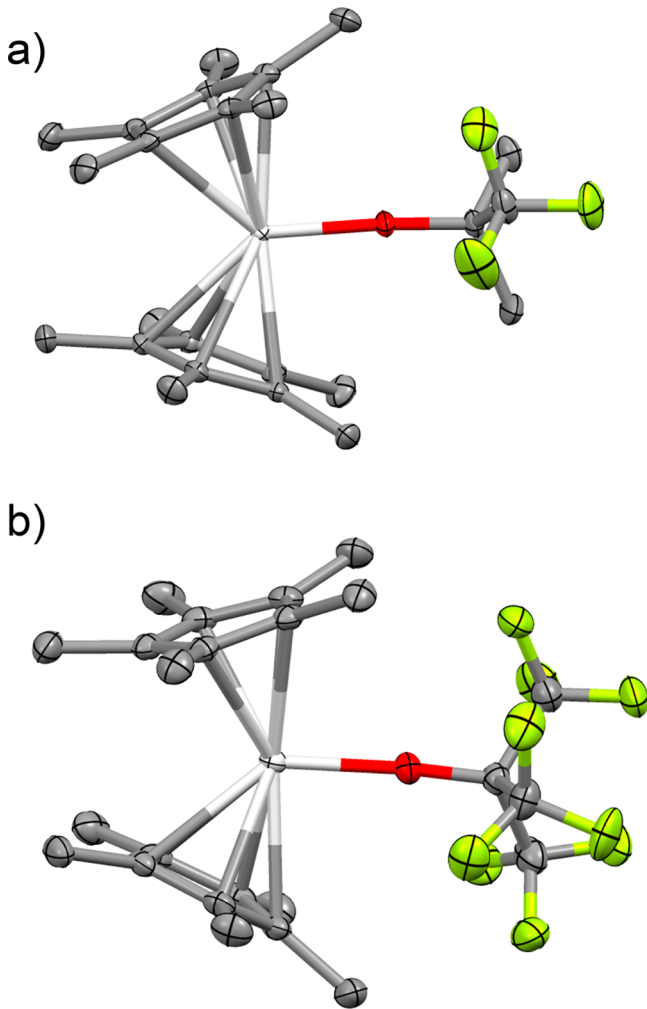
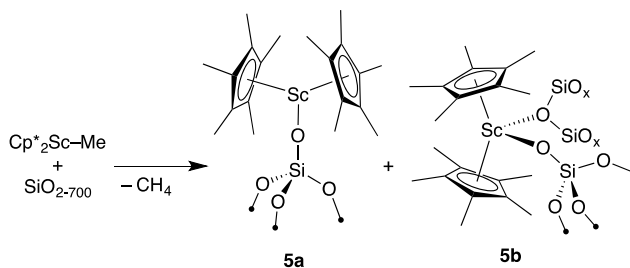
Scheme 2. Synthesis of $\text{Cp}^*_2\text{Sc}-\text{OR}$ Scheme 3. Synthesis of $\text{Cp}^*_2\text{Sc}-\text{OR}$ 

Figure 5. ORTEP drawing of **1** and **3**. Hydrogen atoms omitted for clarity. Refer to the *Supporting Information* for bond distances and angles.

2.199(1) and 2.205(1) Å. These values are similar to known permethylscandocene complexes.

The reaction of SiO_{2-700} and Cp^*_2ScMe results in the formation of methane and $\text{Cp}^*_2\text{ScOSi}\equiv$ (**5a**) and $\text{Cp}^*_2\text{Sc}-(\text{OSi}\equiv)\text{O}(\text{SiO}_x)_2$ (**5b**), **Scheme 3**. This reaction forms 0.23 mmol g⁻¹ methane, which is close to the $-\text{OH}$ loading of SiO_{2-700} (0.26 mmol g⁻¹). The FTIR of **5** contains $\text{sp}^3 \nu_{\text{CH}}$ and $\text{sp}^2 \nu_{\text{CC}}$ bands from the Cp^* fragment (**Figure S9**). In addition, this spectrum shows a significant decrease in the ν_{OH} band associated with isolated and geminal silanols on the partially dehydroxylated silica surface. The ^{13}C CPMAS spectrum of **5**

contains signals at 121.5 and 9.5 ppm that are signatures of the Cp^* ligands in **5** (**Figure S10**). The ^{29}Si CPMAS spectrum of **5** contains only signals for bulk SiO_2 and does not contain signals for alkylsilanes (**Figure S11**). This result indicates that only $\text{HOSi}\equiv$ sites on the partially dehydroxylated silica surface react with Cp^*_2ScMe to form **5** and that side reactions associated with strained siloxane bridges or geminal silanols do not occur under these conditions.⁶⁶ These spectroscopic data do not distinguish between **5a** and **5b**, which is typical of these particular techniques. However, the examples mentioned above and results showing that $\text{Cp}^*_2\text{ScX}(\text{THF})$ complexes ($\text{X} = \text{H}$, alkyl, halide) are isolable,^{41,56} suggest that **5b** would be present on partially dehydroxylated silica surfaces.

Solid-State $^{45}\text{Sc}\{^1\text{H}\}$ NMR of 1–4 and $\text{Cp}^*_2\text{ScOSi}\equiv$. The static $^{45}\text{Sc}\{^1\text{H}\}$ NMR spectra of **1–4** recorded on a 14.1 T NMR spectrometer are shown in **Figure 6**. NMR data acquired at 9.4 T are given in the *Supporting Information* (**Figure S12**). These spectra show characteristic broad second order quadrupolar powder patterns associated with solid-state ^{45}Sc NMR spectra of $\text{Cp}^*_2\text{Sc}-\text{X}$ complexes ($\text{X} = \text{alkyl, halide}$).⁵⁶ Simulations of these spectra are shown in red in **Figure 6**, and the NMR parameters associated with these simulations are summarized in **Table 1**. The C_Q values decrease following the trend **4 > 1 > 2 > 3**.

The static $^{45}\text{Sc}\{^1\text{H}\}$ NMR spectrum of **5** recorded on a 14.1 and 9.4 T spectrometers is shown in **Figure 7**. The $^{45}\text{Sc}\{^1\text{H}\}$ NMR spectrum of **5** is more complicated than the $^{45}\text{Sc}\{^1\text{H}\}$ NMR spectra of **1–4**. There are clear discontinuities in these spectra at both fields indicating that **5** simulates as two sites, which is consistent with the presumption that Cp^*_2ScMe reacts with partially dehydroxylated silica to form **5a** and **5b**. Importantly, the simulated spectral parameters given in **Table 1** are reproduced at both fields, which support simulating this spectrum with two sites. On the basis of the data obtained for **1–4**, all of which have C_Q values >29 MHz, the broad $^{45}\text{Sc}\{^1\text{H}\}$ NMR signal that simulates with an average C_Q of 35.4(4) MHz is assigned to **5a**. The narrower signal that simulates with an average C_Q of 21.9(3) MHz is assigned to **5b**. Below DFT calculations of **1–4**, and small models of **5a** and **5b**, will be described to support these assignments.

DFT Studies of 1–5. Crystallographically characterized **1** and **3** show typical structural features associated with C_{2v} bent metallocenes, and are useful reference points to calibrate DFT studies. The structures of **1–4** were optimized with the B3LYP functional at the 6-311G**(Sc)/6-31G*(C, H, O, F, Si) level of theory. The bond angles and distances obtained from these optimizations are given in **Table 2**. The bond distances and angles of **1** and **3** agree well with the values obtained from the DFT structures. The structures of **2** and **4** are qualitatively similar to **1** and **3**; these structures also adopt C_{2v} structures with $\text{Sc}-\text{O}-\text{C}$ or $\text{Sc}-\text{O}-\text{Si}$ bond angles that are nearly linear.

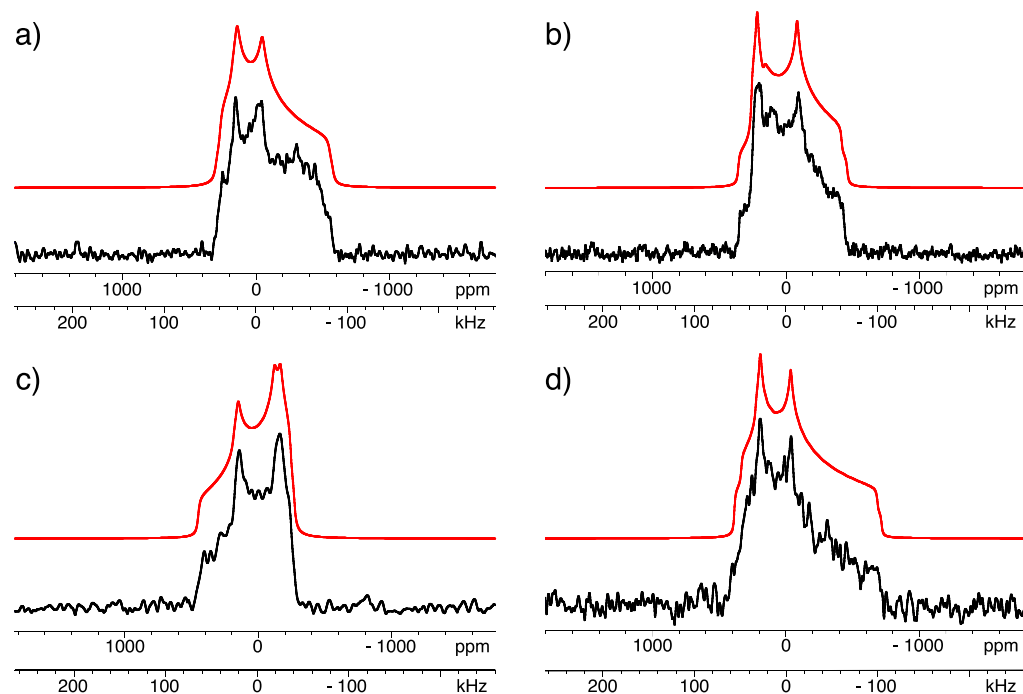


Figure 6. Static solid-state $^{45}\text{Sc}\{^1\text{H}\}$ NMR spectra of **1** (a), **2** (b), **3** (c), and **4** (d) acquired at 14.1 T. The experimental spectra are shown in black and simulations are shown in red.

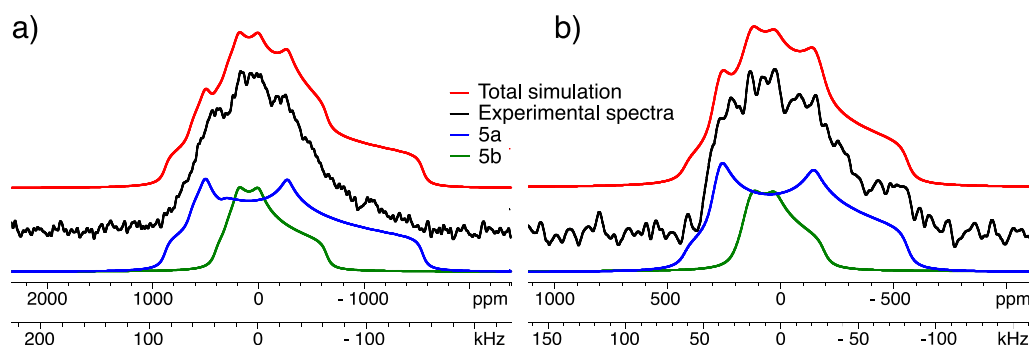


Figure 7. Static $^{45}\text{Sc}\{^1\text{H}\}$ NMR spectrum of **5** at 9.4 T (a) and 14.1 T (b). The experimental spectra are shown in black. Simulations of **5a** are shown in blue, simulations of **5b** are shown in green, and the total simulation is shown in red.

Table 2. Geometrical Parameters from DFT Optimized Structures of $\text{Cp}^*_2\text{Sc}-\text{OR}$

compound	$\text{Cp}^*_a\text{-Sc}$ (Å)	$\text{Cp}^*_b\text{-Sc}$ (Å)	$\text{Cp}^*_a\text{-Sc-Cp}^*_b$ (deg)	Sc-O (Å)	$\text{Cp}^*_a\text{-Sc-O}$ (deg)	$\text{Cp}^*_b\text{-Sc-O}$ (deg)	Sc-O-C (deg)
2	2.23	2.23	135.0	1.94	111.9	113.1	175.5
1	2.22	2.23	134.3	1.98	111.4	114.4	172.3
3	2.21	2.22	134.4	2.02	111.5	114.1	175.4
4	2.21	2.21	137.8	1.96	110.2	112.0	174.0
6a	2.20	2.20	140.5	1.97	109.3	110.2	160.7
6b	2.24	2.24	138.4	2.04	106.9	109.0	106.1

Two models for **5a** and **5b**, $\text{Cp}^*_2\text{Sc}(\kappa^1\text{-OSi(OMe)}_3)$ (**6a**) and $\text{Cp}^*_2\text{Sc}(\kappa^2\text{-OSi(OMe)}_3)$ (**6b**), were optimized at the same level of theory and are shown in Figure 8. Similar to **1–4**, **6a** and **6b** adopt bent metallocene structures. The Sc-O distance in **6a** is 1.97 Å, which is shorter than the Sc-O distance in **6b** (2.04 Å). The Sc-O-Si bond angle in **6a** is 160.7° , which is smaller than the Sc-O-C or Sc-O-Si bond angle for **1–4**. The κ^2 structure in **6b** has a Sc-O-Si bond angle of 106.1° , which is expected.

The $^{45}\text{Sc}\{^1\text{H}\}$ NMR results described above show that $\text{Cp}^*_2\text{Sc-OR}$ complexes are characterized by fairly large C_Q values. The NMR parameters of **1–4** and **6** were calculated at the B3LYP/DZ level of theory, with silicon described with the DZP basis set. The results from these calculations are summarized in Table 3. Trends in C_Q and chemical shift (δ) are similar to those obtained experimentally. At this level of theory, the span values (Ω) are predicted to follow **4 > 1 > 2 > 3**. However, the experimental Ω values do not follow an

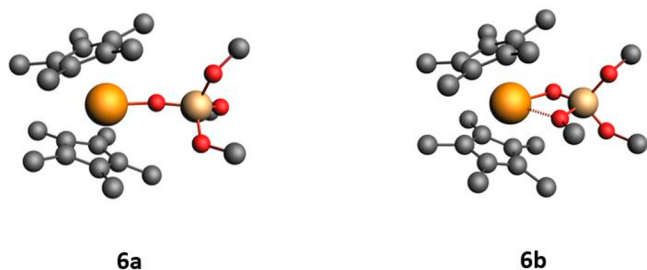


Figure 8. Structures of **6a** and **6b** from DFT calculations.

obvious trend. The calculated Euler angles, which are defined as the angles between the shielding and EFG tensors, are close to those needed to simulate the experimental spectra shown in Figures 6–7 and summarized in Table 1. The calculated C_Q for **6a** is -36.6 MHz, and is close to the C_Q value for **5a**. This value is also close to the experimental and predicted values for **4**. The calculated C_Q for **6b** is 25.8 MHz, significantly smaller than the calculated C_Q for **6a**. This result is consistent with a large C_Q value for **5a**, corresponding to $\text{Cp}^*{}^2\text{Sc}(\kappa^1\text{-OSi}\equiv)$, and a smaller C_Q value for **5b**, which contains an additional interaction with a nearby siloxane bridge to form $\text{Cp}^*{}^2\text{Sc}(\text{OSi}\equiv)\text{O}(\text{SiO}_x)_2$. These results indicate that C_Q derived from ^{45}Sc NMR measurements can distinguish between κ^1 or κ^2 geometries in **5a** and **5b**.

The smaller C_Q for **5b** and **6b** than in **5a** and **6a** is reminiscent of similar trends observed in $\text{Cp}^*{}^2\text{Sc}-\text{X}$ and $\text{Cp}^*{}^2\text{ScX}(\text{THF})$ ($\text{X} = \text{F, Cl, Br, I}$).⁵⁶ In this study the THF adducts consistently show smaller C_Q values than the base free compounds. This is a consequence of the more tetrahedral geometry at scandium in $\text{Cp}^*{}^2\text{ScX}(\text{THF})$, which results in π -overlap between group fragment orbitals in these compounds. This interaction is absent in the THF free $\text{Cp}^*{}^2\text{Sc}-\text{X}$ compounds. This suggests that similar electronic consequences would emerge from analysis of the origin of the C_Q in **6a** and **6b**.

The orientation of the EFG tensor for **1** is shown in Figure 9a. The orientation of **2–4** and **6a** have similar orientations, and are shown in Figure S13. The magnitude of C_Q is determined by eq 2, and depends on V_{33} , the largest contributor to the EFG tensor (eq 1). In **1**, the orientation of V_{33} is perpendicular to the Sc–O bond, which aligns V_{33} with the LUMO of **1**, shown in Figure 9b. The orientation of the EFG tensor in **6b** is shown in Figure 9c. In this case, V_{33} orients along the Sc–O bond (Figure 9c). The calculated LUMO in **6b** is shown in Figure 5d, and corresponds to a π^* -bonding orbital between an oxygen lone pair and the empty orbital on scandium. The LUMO and EFG tensor orientation in **1**, as well as **2–4** and **6a**, is similar to $\text{Cp}^*{}^2\text{Sc}-\text{X}$, while the LUMO and EFG tensor orientation in **6b** is similar to $\text{Cp}^*{}^2\text{ScX}(\text{THF})$ ($\text{X} = \text{F, Cl, Br, I}$).⁵⁶

Table 3. Calculated NMR Parameters for **1–4** and **6**

R	δ_{iso} (ppm)	C_Q (MHz)	η	Ω (ppm)	κ	α (deg)	β (deg)	γ (deg)
1	81	-32.8	1.0	288	0.09	90.9	89.0	87.5
2	108	-31.2	0.75	395	0.06	90.1	88.6	90.0
3	139	-30.3	0.46	520	0.11	89.1	90.3	86.5
4	93	35.4	0.99	270	0.05	89.1	90.3	86.5
6a	90	-36.6	0.93	342	0.07	104.2	88.5	90.4
6b	48	25.8	0.84	238	0.70	89.4	90.8	86.6

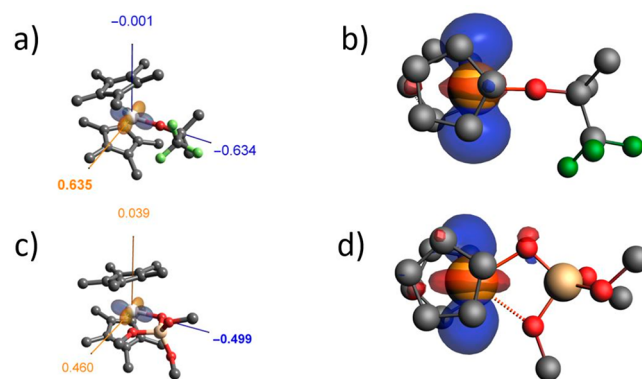


Figure 9. EFG Tensor plots of **1** (a) and **6b** (c). Calculated LUMO of **1** (b) and **6b** (d) calculated at B3LYP/DZ, Si(DZP); isovalue = 0.04.

The C_Q originates from the interaction of the quadrupolar moment of the scandium nucleus and the EFG tensor, which is sensitive to local structure. This coupling is electric in origin, indicating that the magnitude of V_{33} will be related to core and valence scandium orbitals. DFT methods decompose the contributions of V_{33} into Natural Localized Molecular Orbitals (NLMO).⁵⁷ This method is particularly valuable to distinguish how certain geometries, which relate to bonding characteristics, affect V_{33} .^{50,51,57} The NLMO decomposition of V_{33} for **1–4** and **6** is shown in Figure 10a. Consistent with the

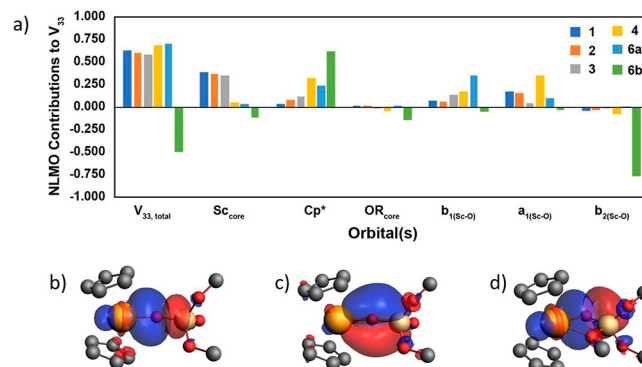


Figure 10. NLMO contributions to V_{33} calculated at B3LYP/DZ, Si(DZP) for **1–4** and **6** (a); plots of valence NLMO for the Sc–O σ -bond in **6a** (b); for the Sc–O π -bond in **6a** (c); and the Sc–O bond in **6b** (d); isovalue = 0.01.

electronic argument, the major contributors to V_{33} are bonding orbitals between scandium and the Cp^* ligand, as well as σ - and π -bonding orbitals that describe the Sc–O bond, shown in Figure 10b and c for **6a** and Figure 10d for **6b**.

In **1–3**, the scandium core orbitals are significant contributors to V_{33} . Filled core scandium orbitals are spherically symmetrical and should not contribute to V_{33} .

Nonzero contributions to C_Q from core orbitals is a result of Sternheimer shielding,⁶⁷ which relates to the anisotropic shielding of nuclear charge by outer core orbitals from bonding partners and polarizability.⁵⁰ However, the electronics of the alkoxide also clearly play a role in the contributions to V_{33} . As the alkoxide becomes more electron withdrawing the σ -bonding Sc–O orbital (a_1) contributes less to V_{33} .

Figure 10a shows that the contributors to V_{33} in **4** and **6a**, closely related molecular structures to **5a**, are rather different than the contributions to V_{33} in **6b**, which is the model for **5b**. In **4** and **6a**, the major valence contributions are from the $Cp^*_{\text{2}}\text{Sc}$, of roughly equal magnitude, and the Sc–OSiR₃ σ - and π -bonds (a_1 and b_1). In **6b**, the $Cp^*_{\text{2}}\text{Sc}$ orbitals are major contributors, but the a_1 and b_1 orbitals are minor contributors to V_{33} because this compound adopts a $\kappa^2\text{-OSi(OMe)}_3$ ligand geometry. Rather the b_2 orbital is the major contributor to V_{33} in **6b**. These results show that the magnitude of C_Q for these complexes can differentiate between κ^1 - and κ^2 -geometries and that the origin of the C_Q in these geometries is related to different valence orbitals.

CONCLUSIONS

This study was motivated by the application of $^{45}\text{Sc}\{^1\text{H}\}$ NMR parameters to determine the structure of surface organo-scandium sites supported on partially dehydroxylated silica. The reaction of $Cp^*_{\text{2}}\text{ScMe}$ and SiO_{2-700} was chosen because the supported $Cp^*_{\text{2}}\text{Sc}$ -fragment contains bulky Cp^* ligands to enforce monomeric speciation in solution. This avoids complications associated with formation of aggregates during the grafting reaction, which can complicate analysis of the solid-state NMR data in some cases.^{43,59,60} The bent metallocene C_{2v} geometry of the $Cp^*_{\text{2}}\text{Sc}$ -fragment allows access to only two possible conformations of the organo-scandium species on the silica surface ($Cp^*_{\text{2}}\text{ScOSi}\equiv$ (**5a**) and $Cp^*_{\text{2}}\text{Sc(OSi}\equiv)\text{O(SiO}_x)_2$ (**5b**)). Consistent with this hypothesis, two sites were needed to accurately fit the solid-state $^{45}\text{Sc}\{^1\text{H}\}$ NMR data of **5**. One of the sites had a large C_Q assigned to **5a**, and the other site had a significantly smaller C_Q assigned to **5b**.

The $^{45}\text{Sc}\{^1\text{H}\}$ NMR parameters of $Cp^*_{\text{2}}\text{Sc-OR}$ (**1–4**) were important benchmarks that were necessary to relate to the $^{45}\text{Sc}\{^1\text{H}\}$ NMR parameters of **5a** and **5b**. These compounds were prepared by straightforward reactions of $Cp^*_{\text{2}}\text{ScMe}$ with alcohols to yield $Cp^*_{\text{2}}\text{Sc-OR}$ and methane. Diffraction studies of $Cp^*_{\text{2}}\text{Sc-OCMe}_2\text{CF}_3$ (**1**) and $Cp^*_{\text{2}}\text{Sc-O(CF}_3)_3$ (**3**) are typical of monomeric C_{2v} , bent metallocenes. **1–4** all show broad quadrupolar powder patterns typical of $Cp^*_{\text{2}}\text{Sc-X}$ (X = halide, alkyl).^{55,56} These compounds also have similar C_Q values to those obtained for **5a**. DFT studies showed that the EFG tensor in $Cp^*_{\text{2}}\text{Sc-OR}$, and a small cluster $Cp^*_{\text{2}}\text{Sc}(\kappa^1\text{-OSi(OMe)}_3)$ (**6a**) to approximate the primary coordination sphere in **5a**, orient the V_{33} component of the EFG tensor perpendicular to the Sc–O bond. This aligns V_{33} with the LUMO of these compounds. NLMO calculations showed that the Sc–O σ - and π -bonding orbitals are contributors to V_{33} in these terminal alkoxides.

These results are in contrast to those for $Cp^*_{\text{2}}\text{Sc}(\kappa^2\text{-OSi(OMe)}_3)$ (**6b**). This compound is a small cluster model of $Cp^*_{\text{2}}\text{Sc(OSi}\equiv)\text{O(SiO}_x)_2$ (**5b**). Though this is a rather dramatic truncation of a silica surface, the calculated C_Q for **6** (25.8 MHz) is rather close to the C_Q of **5b** ($C_Q = 21.9(3)$ MHz) derived from simulations of experimental NMR data.

This result shows that C_Q is sensitive to the primary coordination sphere of scandium, which is typically encountered when modeling NMR properties of quadrupolar nuclei. In **6b**, the V_{33} component of the EFG tensor is not aligned perpendicular to the Sc–O bond, as in the terminal alkoxides **1–4** and **6a**, but rather along the Sc–O bond. NLMO decomposition of V_{33} in **6b** is also quite different from the terminal alkoxides. The Sc–O σ - and π -bonding orbitals are minor contributors to V_{33} . In **6b**, the b_2 orbital is the major contributor to V_{33} because this compound adopts a κ^2 -geometry with the siloxide. These results establish that the magnitude of C_Q and the origin of V_{33} are very sensitive to local structure, in this case the coordination of a -OSi(OMe)_3 ligand in κ^1 - or κ^2 geometries, and support the assignments of **5a** and **5b**. These studies show that quadrupolar NMR properties of surface organoscandium species, when coupled with relevant molecular models and supplemented by DFT studies, can provide valuable information about the structure of these supported organometallic sites.

ASSOCIATED CONTENT

Supporting Information

The Supporting Information is available free of charge at <https://pubs.acs.org/doi/10.1021/acs.organomet.9b00840>.

Chemical structure ([XYZ](#))

NMR spectra, elemental analysis results, IR spectra, coordinates for computations, EFG orientation plots, NLMO tables ([PDF](#))

Accession Codes

CCDC 1971453–1971454 contain the supplementary crystallographic data for this paper. These data can be obtained free of charge via www.ccdc.cam.ac.uk/data_request/cif, or by emailing data_request@ccdc.cam.ac.uk, or by contacting The Cambridge Crystallographic Data Centre, 12 Union Road, Cambridge CB2 1EZ, UK; fax: +44 1223 336033.

AUTHOR INFORMATION

Corresponding Author

Matthew P. Conley – Department of Chemistry, University of California, Riverside, California 92521, United States;
orcid.org/0000-0001-8593-5814;
 Email: matthew.conley@ucr.edu

Authors

Damien B. Culver – Department of Chemistry, University of California, Riverside, California 92521, United States

Winn Huynh – Department of Chemistry, University of California, Riverside, California 92521, United States

Hosein Tafazolian – Department of Chemistry, University of California, Riverside, California 92521, United States

Complete contact information is available at:
<https://pubs.acs.org/10.1021/acs.organomet.9b00840>

Author Contributions

[‡]These authors contributed equally.

Notes

The authors declare no competing financial interest.

ACKNOWLEDGMENTS

M.P.C. is a member of the UCR Center for Catalysis. Financial support for this work was provided by the University of California, Riverside and the National Science Foundation (CHE-1800561). The solid-state NMR measurements for this study were recorded on an instrument supported by the National Science Foundation (CHE-1626673).

REFERENCES

- (1) *Handbook of Heterogeneous Catalysis*, 1st ed.; Wiley-VCH, 1997; p 2800.
- (2) Marks, T. J. Surface-bound metal hydrocarbyls. Organometallic connections between heterogeneous and homogeneous catalysis. *Acc. Chem. Res.* **1992**, *25*, 57–65.
- (3) Wegener, S. L.; Marks, T. J.; Stair, P. C. Design Strategies for the Molecular Level Synthesis of Supported Catalysts. *Acc. Chem. Res.* **2012**, *45*, 206–214.
- (4) Basset, J.-M.; Coperet, C.; Soulivong, D.; Taoufik, M.; Cazat, J. T. Metathesis of Alkanes and Related Reactions. *Acc. Chem. Res.* **2010**, *43*, 323–334.
- (5) Lecuyer, C.; Quignard, F.; Choplin, A.; Olivier, D.; Basset, J.-M. Surface Organometallic Chemistry on Oxides: Selective Catalytic Low-Temperature Hydrogenolysis of Alkanes by a Highly Electrophilic Zirconium Hydride Complex Supported on Silica. *Angew. Chem., Int. Ed. Engl.* **1991**, *30*, 1660–1661.
- (6) Pelletier, J. D. A.; Basset, J.-M. Catalysis by Design: Well-Defined Single-Site Heterogeneous Catalysts. *Acc. Chem. Res.* **2016**, *49*, 664–677.
- (7) Guzman, J.; Gates, B. C. Supported molecular catalysts: metal complexes and clusters on oxides and zeolites. *Dalton Trans.* **2003**, 3303–3318.
- (8) Copéret, C.; Allouche, F.; Chang, K. W.; Conley, M.; Delley, M. F.; Fedorov, A.; Moroz, I.; Mougel, V.; Pucino, M.; Searles, K.; Yamamoto, K.; Zhizhko, P. Bridging the Gap between Industrial and Well-Defined Supported Catalysts. *Angew. Chem., Int. Ed.* **2018**, *57*, 6398–6440.
- (9) Stalzer, M.; Delferro, M.; Marks, T. Supported Single-Site Organometallic Catalysts for the Synthesis of High-Performance Polyolefins. *Catal. Lett.* **2015**, *145*, 3–14.
- (10) Kaphan, D. M.; Klet, R. C.; Perras, F. A.; Pruski, M.; Yang, C.; Kropf, A. J.; Delferro, M. Surface Organometallic Chemistry of Supported Iridium(III) as a Probe for Organotransition Metal–Support Interactions in C–H Activation. *ACS Catal.* **2018**, *8*, 5363–5373.
- (11) Stalzer, M. M.; Nicholas, C. P.; Bhattacharyya, A.; Motta, A.; Delferro, M.; Marks, T. J. Single-Face/All-cis Arene Hydrogenation by a Supported Single-Site d0 Organozirconium Catalyst. *Angew. Chem., Int. Ed.* **2016**, *55*, 5263–5267.
- (12) Gu, W.; Stalzer, M. M.; Nicholas, C. P.; Bhattacharyya, A.; Motta, A.; Gallagher, J. R.; Zhang, G.; Miller, J. T.; Kobayashi, T.; Pruski, M.; Delferro, M.; Marks, T. J. Benzene Selectivity in Competitive Arene Hydrogenation: Effects of Single-Site Catalyst Acidic Oxide Surface Binding Geometry. *J. Am. Chem. Soc.* **2015**, *137*, 6770–6780.
- (13) Klet, R. C.; Kaphan, D. M.; Liu, C.; Yang, C.; Kropf, A. J.; Perras, F. A.; Pruski, M.; Hock, A. S.; Delferro, M. Evidence for Redox Mechanisms in Organometallic Chemisorption and Reactivity on Sulfated Metal Oxides. *J. Am. Chem. Soc.* **2018**, *140*, 6308–6316.
- (14) Syed, Z. H.; Kaphan, D. M.; Perras, F. A.; Pruski, M.; Ferrandon, M. S.; Wegener, E. C.; Celik, G.; Wen, J.; Liu, C.; Dogan, F.; Goldberg, K. I.; Delferro, M. Electrophilic Organoiridium(III) Pincer Complexes on Sulfated Zirconia for Hydrocarbon Activation and Functionalization. *J. Am. Chem. Soc.* **2019**, *141*, 6325–6337.
- (15) Williams, L. A.; Marks, T. J. Synthesis, Characterization, and Heterogeneous Catalytic Implementation of Sulfated Alumina Nanoparticles. Arene Hydrogenation and Olefin Polymerization Properties of Supported Organozirconium Complexes. *ACS Catal.* **2011**, *1*, 238–245.
- (16) Nicholas, C. P.; Ahn, H.; Marks, T. J. Synthesis, Spectroscopy, and Catalytic Properties of Cationic Organozirconium Adsorbates on Super Acidic Sulfated Alumina. Single-Site Heterogeneous Catalysts with Virtually 100% Active Sites. *J. Am. Chem. Soc.* **2003**, *125*, 4325–4331.
- (17) Ahn, H.; Nicholas, C. P.; Marks, T. J. Surface organozirconium electrophiles activated by chemisorption on "super acidic" sulfated zirconia as hydrogenation and polymerization catalysts. A synthetic, structural, and mechanistic catalytic study. *Organometallics* **2002**, *21*, 1788–1806.
- (18) Rodriguez, J.; Culver, D. B.; Conley, M. P. Generation of Phosphonium Sites on Sulfated Zirconium Oxide: Relationship to Brønsted Acid Strength of Surface – OH Sites. *J. Am. Chem. Soc.* **2019**, *141*, 1484–1488.
- (19) Culver, D. B.; Tafazolian, H.; Conley, M. P. A Bulky Pd(II) α -Diimine Catalyst Supported on Sulfated Zirconia for the Polymerization of Ethylene and Copolymerization of Ethylene and Methyl Acrylate. *Organometallics* **2018**, *37*, 1001–1006.
- (20) Tafazolian, H.; Culver, D. B.; Conley, M. P. A Well-Defined Ni(II) α -Diimine Catalyst Supported on Sulfated Zirconia for Polymerization Catalysis. *Organometallics* **2017**, *36*, 2385–2388.
- (21) Williams, L. A.; Guo, N.; Motta, A.; Delferro, M.; Fragala, I. L.; Miller, J. T.; Marks, T. J. Surface structural-chemical characterization of a single-site d0 heterogeneous arene hydrogenation catalyst having 100% active sites. *Proc. Natl. Acad. Sci. U. S. A.* **2013**, *110*, 413–418.
- (22) Blanc, F.; Coperet, C.; Lesage, A.; Emsley, L. High resolution solid state NMR spectroscopy in surface organometallic chemistry: access to molecular understanding of active sites of well-defined heterogeneous catalysts. *Chem. Soc. Rev.* **2008**, *37*, 518–526.
- (23) Copéret, C.; Liao, W.-C.; Gordon, C. P.; Ong, T.-C. Active Sites in Supported Single-Site Catalysts: An NMR Perspective. *J. Am. Chem. Soc.* **2017**, *139*, 10588–10596.
- (24) Reed, C. A. The Silylum Ion Problem, R₃Si⁺. Bridging Organic and Inorganic Chemistry. *Acc. Chem. Res.* **1998**, *31*, 325–332.
- (25) Xie, Z.; Manning, J.; Reed, R. W.; Mathur, R.; Boyd, P. D. W.; Benesi, A.; Reed, C. A. Approaching the Silylum (R₃Si⁺) Ion: Trends with Hexahalo (Cl, Br, I) Carboranes as Counterions. *J. Am. Chem. Soc.* **1996**, *118*, 2922–2928.
- (26) Ramírez-Contreras, R.; Bhuvanesh, N.; Zhou, J.; Ozerov, O. V. Synthesis of a Silylum Zwitterion. *Angew. Chem., Int. Ed.* **2013**, *52*, 10313–10315.
- (27) Küppers, T.; Bernhardt, E.; Eujen, R.; Willner, H.; Lehmann, C. W. [Me₃Si][R-CB₁₁F₁₁]—Synthesis and Properties. *Angew. Chem., Int. Ed.* **2007**, *46*, 6346–6349.
- (28) Anwander, R.; Nagl, I.; Widenmeyer, M.; Engelhardt, G. n.; Groeger, O.; Palm, C.; Roser, T. Surface Characterization and Functionalization of MCM-41 Silicas via Silazane Silylation. *J. Phys. Chem. B* **2000**, *104*, 3532–3544.
- (29) Zapilko, C.; Widenmeyer, M.; Nagl, I.; Estler, F.; Anwander, R.; Raudaschl-Sieber, G.; Groeger, O.; Engelhardt, G. Advanced Surface Functionalization of Periodic Mesoporous Silica: Kinetic Control by Trisilazane Reagents. *J. Am. Chem. Soc.* **2006**, *128*, 16266–16276.
- (30) Conley, M. P.; Drost, R. M.; Baffert, M.; Gajan, D.; Elsevier, C.; Franks, W. T.; Oschkinat, H.; Veyre, L.; Zagdoun, A.; Rossini, A.; Lelli, M.; Lesage, A.; Casano, G.; Ouardi, O.; Tordo, P.; Emsley, L.; Copéret, C.; Thieuleux, C. A Well-Defined Pd Hybrid Material for the Z-Selective Semihydrogenation of Alkynes Characterized at the Molecular Level by DNP SENS. *Chem. - Eur. J.* **2013**, *19*, 12234–12238.
- (31) Bluemel, J. Reactions of Ethoxysilanes with Silica: A Solid-State NMR Study. *J. Am. Chem. Soc.* **1995**, *117*, 2112–2113.
- (32) Culver, D. B.; Conley, M. P. Activation of C–F Bonds by Electrophilic Organosilicon Sites Supported on Sulfated Zirconia. *Angew. Chem., Int. Ed.* **2018**, *57*, 14902–14905.
- (33) Culver, D. B.; Venkatesh, A.; Huynh, W.; Rossini, A. J.; Conley, M. P. Al(ORF)₃ (RF = C(CF₃)₃) activated silica: a well-defined weakly coordinating surface anion. *Chem. Sci.* **2020**, *11*, 1510–1517.
- (34) Millot, N.; Soignier, S.; Santini, C. C.; Baudouin, A.; Basset, J.-M. Synthesis, Characterization, and Activity in Ethylene Polymer-

ization of Silica Supported Cationic Cyclopentadienyl Zirconium Complexes. *J. Am. Chem. Soc.* **2006**, *128*, 9361–9370.

(35) Le Roux, E.; Chabanas, M.; Baudouin, A.; de Mallmann, A.; Copéret, C.; Quadrelli, E. A.; Thivolle-Cazat, J.; Basset, J.-M.; Lukens, W.; Lesage, A.; Emsley, L.; Sunley, G. J. Detailed Structural Investigation of the Grafting of $[\text{Ta}(\text{CHtBu})(\text{CH2tBu})_3]$ and $[\text{Cp}^*\text{TaMe}_4]$ on Silica Partially Dehydroxylated at 700 oC and the Activity of the Grafted Complexes toward Alkane Metathesis. *J. Am. Chem. Soc.* **2004**, *126*, 13391–13399.

(36) Rhers, B.; Salameh, A.; Baudouin, A.; Quadrelli, E. A.; Taoufik, M.; Copéret, C.; Lefebvre, F.; Basset, J.-M.; Solans-Monfort, X.; Eisenstein, O.; Lukens, W. W.; Lopez, L. P. H.; Sinha, A.; Schrock, R. R. A Well-Defined, Silica-Supported Tungsten Imido Alkylidene Olefin Metathesis Catalyst. *Organometallics* **2006**, *25*, 3554–3557.

(37) Conley, M. P.; Lepadula, G.; Sanders, K.; Gajan, D.; Lesage, A.; del Rosal, I.; Maron, L.; Lukens, W. W.; Copéret, C.; Andersen, R. A. The Nature of Secondary Interactions at Electrophilic Metal Sites of Molecular and Silica-Supported Organolutetium Complexes from Solid-State NMR Spectroscopy. *J. Am. Chem. Soc.* **2016**, *138*, 3831–3843.

(38) Chabanas, M.; Baudouin, A.; Copéret, C.; Basset, J.-M.; Lukens, W.; Lesage, A.; Hediger, S.; Emsley, L. Perhydrocarbyl ReVII Complexes: Comparison of Molecular and Surface Complexes. *J. Am. Chem. Soc.* **2003**, *125*, 492–504.

(39) Mazoyer, E.; Merle, N.; Mallmann, A. d.; Basset, J.-M.; Berrier, E.; Delevoye, L.; Paul, J.-F.; Nicholas, C. P.; Gauvin, R. M.; Taoufik, M. Development of the first well-defined tungsten oxo alkyl derivatives supported on silica by SOMC: towards a model of WO_3/SiO_2 olefin metathesis catalyst. *Chem. Commun.* **2010**, *46*, 8944–8946.

(40) A notable exception to this trend was encountered in ^{13}C CPMAS NMR studies of TaCl_2Me_3 supported on partially dehydroxylated silica: Chen, Y.; Callens, E.; Abou-Hamad, E.; Merle, N.; White, A. J. P.; Taoufik, M.; Copéret, C.; Le Roux, E.; Basset, J. M. $(\text{SiO})(\text{TaCl}_2\text{Me}_2)\text{-Cl-V}$: A Well-Defined Silica-Supported Tantalum(V) Surface Complex as Catalyst Precursor for the Selective Cocatalyst-Free Trimerization of Ethylene. *Angew. Chem., Int. Ed.* **2012**, *51*, 11886–11889.

(41) Thompson, M. E.; Baxter, S. M.; Bulls, A. R.; Burger, B. J.; Nolan, M. C.; Santarsiero, B. D.; Schaefer, W. P.; Bercaw, J. E. sigma-Bond metathesis for carbon-hydrogen bonds of hydrocarbons and $\text{Sc}-\text{R}$ ($\text{R} = \text{H}$, alkyl, aryl) bonds of permethylscandocene derivatives. Evidence for noninvolvement of the π -system in electrophilic activation of aromatic and vinylic C-H bonds. *J. Am. Chem. Soc.* **1987**, *109*, 203–219.

(42) Ashbrook, S. E.; Sneddon, S. New Methods and Applications in Solid-State NMR Spectroscopy of Quadrupolar Nuclei. *J. Am. Chem. Soc.* **2014**, *136*, 15440–15456.

(43) Kermagoret, A.; Kerber, R. N.; Conley, M. P.; Callens, E.; Florian, P.; Massiot, D.; Copéret, C.; Delbecq, F.; Rozanska, X.; Sautet, P. Triisobutylaluminum: bulkier and yet more reactive towards silica surfaces than triethyl or trimethylaluminum. *Dalton Trans.* **2013**, *42*, 12681–12687.

(44) Merle, N.; Girard, G.; Popoff, N.; De Mallmann, A.; Bouhouste, Y.; Trebosc, J.; Berrier, E.; Paul, J.-F.; Nicholas, C. P.; Del Rosal, I.; Maron, L.; Gauvin, R. M.; Delevoye, L.; Taoufik, M. On the Track to Silica-Supported Tungsten Oxo Metathesis Catalysts: Input from ^{17}O Solid-State NMR. *Inorg. Chem.* **2013**, *52*, 10119–10130.

(45) Merle, N.; Trebosc, J.; Baudouin, A.; Rosal, I. D.; Maron, L.; Szeto, K.; Genelot, M.; Mortreux, A.; Taoufik, M.; Delevoye, L.; Gauvin, R. M. ^{17}O NMR Gives Unprecedented Insights into the Structure of Supported Catalysts and Their Interaction with the Silica Carrier. *J. Am. Chem. Soc.* **2012**, *134*, 9263–9275.

(46) Grekov, D.; Vancompernolle, T.; Taoufik, M.; Delevoye, L.; Gauvin, R. M. Solid-state NMR of quadrupolar nuclei for investigations into supported organometallic catalysts: scope and frontiers. *Chem. Soc. Rev.* **2018**, *47*, 2572–2590.

(47) O'Keefe, C. A.; Johnston, K. E.; Sutter, K.; Autschbach, J.; Gauvin, R.; Trébosc, J.; Delevoye, L.; Popoff, N.; Taoufik, M.; Oudatchin, K.; Schurko, R. W. An Investigation of Chlorine Ligands in Transition-Metal Complexes via ^{35}Cl Solid-State NMR and Density Functional Theory Calculations. *Inorg. Chem.* **2014**, *53*, 9581–9597.

(48) Medek, A.; Frydman, V.; Frydman, L. Central Transition Nuclear Magnetic Resonance in the Presence of Large Quadrupole Couplings: Cobalt-59 Nuclear Magnetic Resonance of Cobaltophthalocyanines. *J. Phys. Chem. A* **1999**, *103*, 4830–4835.

(49) Schurko, R. W. Ultra-Wideline Solid-State NMR Spectroscopy. *Acc. Chem. Res.* **2013**, *46*, 1985–1995.

(50) Autschbach, J.; Zheng, S.; Schurko, R. W. Analysis of electric field gradient tensors at quadrupolar nuclei in common structural motifs. *Concepts Magn. Reson., Part A* **2010**, *36A*, 84–126.

(51) Srebro, M.; Autschbach, J. Computational Analysis of $^{47}/^{49}\text{Ti}$ NMR Shifts and Electric Field Gradient Tensors of Half-Titanocene Complexes: Structure–Bonding–Property Relationships. *Chem. - Eur. J.* **2013**, *19*, 12018–12033.

(52) Rossini, A. J.; Schurko, R. W. Experimental and Theoretical Studies of ^{45}Sc NMR Interactions in Solids. *J. Am. Chem. Soc.* **2006**, *128*, 10391–10402.

(53) Giovine, R.; Volkringer, C.; Ashbrook, S. E.; Trébosc, J.; McKay, D.; Loiseau, T.; Amoureaux, J.-P.; Lafon, O.; Pourpoint, F. Solid-State NMR Spectroscopy Proves the Presence of Penta-coordinated Sc Sites in MIL-100(Sc). *Chem. - Eur. J.* **2017**, *23*, 9525–9534.

(54) Vancompernolle, T.; Trivelli, X.; Delevoye, L.; Pourpoint, F.; Gauvin, R. M. On the use of solid-state ^{45}Sc NMR for structural investigations of molecular and silica-supported scandium amide catalysts. *Dalton Trans.* **2017**, *46*, 13176–13179.

(55) Culver, D. B.; Huynh, W.; Tafazolian, H.; Ong, T.-C.; Conley, M. P. The β -Agostic Structure in $(\text{CSMe}_5)2\text{Sc}(\text{CH}_2\text{CH}_3)$: Solid-State NMR Studies of $(\text{CSMe}_5)2\text{Sc}-\text{R}$ ($\text{R} = \text{Me, Ph, Et}$). *Angew. Chem., Int. Ed.* **2018**, *57*, 9520–9523.

(56) Huynh, W.; Culver, D. B.; Tafazolian, H.; Conley, M. P. Solid-state ^{45}Sc NMR studies of $\text{Cp}^*2\text{Sc}-\text{X}$ and $\text{Cp}^*2\text{ScX}(\text{THF})$. *Dalton Transactions* **2018**, *47*, 13063–13071.

(57) Rossini, A. J.; Mills, R. W.; Briscoe, G. A.; Norton, E. L.; Geier, S. J.; Hung, I.; Zheng, S.; Autschbach, J.; Schurko, R. W. Solid-State Chlorine NMR of Group IV Transition Metal Organometallic Complexes. *J. Am. Chem. Soc.* **2009**, *131*, 3317–3330.

(58) Rimola, A.; Costa, D.; Sodupe, M.; Lambert, J.-F.; Ugliengo, P. Silica Surface Features and Their Role in the Adsorption of Biomolecules: Computational Modeling and Experiments. *Chem. Rev.* **2013**, *113*, 4216–4313.

(59) Kerber, R. N.; Kermagoret, A.; Callens, E.; Florian, P.; Massiot, D.; Lesage, A.; Copéret, C.; Delbecq, F.; Rozanska, X.; Sautet, P. Nature and Structure of Aluminum Surface Sites Grafted on Silica from a Combination of High-Field Aluminum-27 Solid-State NMR Spectroscopy and First-Principles Calculations. *J. Am. Chem. Soc.* **2012**, *134*, 6767–6775.

(60) Kermagoret, A.; Kerber, R. N.; Conley, M. P.; Callens, E.; Florian, P.; Massiot, D.; Delbecq, F. B.; Rozanska, X.; Copéret, C.; Sautet, P. Chlorodiethylaluminum supported on silica: A dinuclear aluminum surface species with bridging u2-Cl-ligand as a highly efficient co-catalyst for the Ni-catalyzed dimerization of ethene. *J. Catal.* **2014**, *313*, 46–54.

(61) Poater, A.; Solans-Monfort, X.; Clot, E.; Copéret, C.; Eisenstein, O. Understanding d0-Olefin Metathesis Catalysts: Which Metal, Which Ligands? *J. Am. Chem. Soc.* **2007**, *129*, 8207–8216.

(62) Solans-Monfort, X.; Clot, E.; Copéret, C.; Eisenstein, O. d0 Re-Based Olefin Metathesis Catalysts, $\text{Re}(\text{=CR})(\text{CHR})(\text{X})(\text{Y})$: The Key Role of X and Y Ligands for Efficient Active Sites. *J. Am. Chem. Soc.* **2005**, *127*, 14015–14025.

(63) Estes, D. P.; Gordon, C. P.; Fedorov, A.; Liao, W. C.; Ehrhorn, H.; Bittner, C.; Zier, M. L.; Bockfeld, D.; Chan, K. W.; Eisenstein, O.; Raynaud, C.; Tamm, M.; Copéret, C. Molecular and Silica-Supported Molybdenum Alkyne Metathesis Catalysts: Influence of Electronics and Dynamics on Activity Revealed by Kinetics, Solid-State NMR,

and Chemical Shift Analysis. *J. Am. Chem. Soc.* **2017**, *139*, 17597–17607.

(64) Halbert, S.; Coperet, C.; Raynaud, C.; Eisenstein, O. Elucidating the Link between NMR Chemical Shifts and Electronic Structure in d(0) Olefin Metathesis Catalysts. *J. Am. Chem. Soc.* **2016**, *138*, 2261–2272.

(65) Young, R. P.; Lewis, C. R.; Yang, C.; Wang, L.; Harper, J. K.; Mueller, L. J. TensorView: A software tool for displaying NMR tensors. *Magn. Reson. Chem.* **2019**, *57*, 211–223.

(66) Conley, M. P.; Rossini, A. J.; Comas-Vives, A.; Valla, M.; Casano, G.; Ouari, O.; Tordo, P.; Lesage, A.; Emsley, L.; Coperet, C. Silica-surface reorganization during organotin grafting evidenced by Sn-119 DNP SENS: a tandem reaction of gem-silanols and strained siloxane bridges. *Phys. Chem. Chem. Phys.* **2014**, *16*, 17822–17827.

(67) Lucken, E. A. C. *Nuclear Quadrupole Coupling Constants*; Academic Press, 1969.